Fluid Dynamics & Materials Processing

Tech Science Press

http://doi.org/10.32604/fdmp.2026.086917

ARTICLE

A Novel Grooved-Tooth Rotary Cavitation Generator for Enhanced Hydrodynamic Cavitation and Wastewater Treatment

Hong Qi[1], Jun Zhang[1,*], Xinyao Hu[2], Liming Qian[1] and Peiyu He[2,*]

[1]School of Mechanical Engineering, Nantong Institute of Technology, Nantong, China
[2]School of Mechanical Engineering, Jiangsu University, Zhenjiang, China
*Corresponding Authors: Jun Zhang. Email: 20110007@ntit.edu.cn; Peiyu He. Email: hepeiyu@ujs.edu.cn

Received: 09 June 2026; Accepted: 17 August 2026; Published: 04 September 2026

ABSTRACT: This study presents a novel grooved-tooth rotary cavitation generator (GRCG) and systematically investigates its hydrodynamic cavitation and wastewater treatment response through a combination of three-dimensional transient numerical simulations and experimental validation. The simulations, based on the Realizable k-ε turbulence model and the Zwart-Gerber-Belamri cavitation model, are used to examine the influence of radial clearance (L) and rotational speed (N) on cavitation development. The numerical predictions are validated through Escherichia coli inactivation and Rhodamine B degradation experiments. The results show that decreasing the radial clearance and increasing the rotational speed markedly enhance cavitation intensity. At L = 1 mm and N = 4500 r/min, the total vapor volume reaches its maximum, corresponding to a Rhodamine B degradation efficiency of 43.6%, significantly higher than that achieved at larger clearances. The Escherichia coli concentration decreases progressively throughout the treatment, demonstrating the strong bactericidal performance of the proposed device. The grooved-tooth geometry promotes micro-vortex formation, strengthening the synergistic effects of mechanical shear and oxidative degradation, thereby improving cavitation efficiency. The close agreement between the simulated vapor volume and the experimental degradation results confirms the reliability of the numerical model.

KEYWORDS: Hydrodynamic cavitation; rotary generator; grooved-tooth; numerical simulation; wastewater treatment

1 Introduction

The rapid advancement of global industrialization and urbanization has led to an exponential increase in water demand, simultaneously exacerbating the crisis of water scarcity and persistent environmental pollution. Modern wastewater, originating from complex industrial processes, intensive agricultural runoff, and expanding municipal discharge, contains a diverse array of recalcitrant organic pollutants, such as phenolic compounds, synthetic dyes, pesticides, and antibiotics. These contaminants are characterized by their stable heterocyclic molecular structures and high resistance to conventional biological and chemical treatment methods [1–3]. If left untreated, these substances accumulate in aquatic ecosystems and enter the human food chain through biomagnification, posing severe long-term threats to public health and ecological integrity. Although existing purification technologies, including physical retention, chemical precipitation, and traditional biological oxidation, are widely implemented, they often encounter bottlenecks when dealing with high-concentration, non-biodegradable effluents, such as high operational costs, low mineralized rates, and the secondary risk of sludge disposal. Consequently, developing efficient, economical, and environmentally friendly Advanced Oxidation Processes (AOPs) has become a top priority in environmental engineering.

Hydrodynamic cavitation (HC) has emerged as a revolutionary AOP candidate for the remediation of these persistent pollutants [4–6]. HC refers to the formation, growth, and subsequent violent collapse of micro-bubbles (cavities) in a liquid medium when the local static pressure drops below the saturation vapor pressure at a constant temperature. This transient process occurs within microseconds, releasing a tremendous amount of energy and creating localized "hotspots" characterized by extreme temperatures (up to 5000 K) and intense pressures (exceeding 100 MPa). These extreme physical conditions trigger the homolytic cleavage of water molecules, yielding highly reactive species, most notably hydroxyl radicals (·OH), which possess a superior oxidation potential for the mineralization of organic molecules into CO_2 and H_2O [7,8]. Beyond chemical oxidation, the shockwaves and high-velocity micro-jets produced during bubble collapse provide intense mechanical shear, which physically disrupts macromolecular structures and enhances mass transfer across the gas-liquid interface [9,10]. Compared to other AOPs like Ozonation or Fenton processes, HC is distinguished by its lack of chemical additives, moderate overall reaction conditions, and significant potential for large-scale industrial integration.

In practical engineering, HC was traditionally induced by static devices, such as orifice plates or Venturi tubes [11,12]. However, the cavitation intensity in these static configurations is strictly constrained by the fixed geometric dimensions and the requisite upstream pressure, leading to limited operational flexibility and a high risk of clogging. To transcend these limitations, Rotary Cavitation Generators (RCGs) have been developed, utilizing rotating components like hole-rimmed disks or vaned rotors to generate intense shear force fields and unsteady pressure pulsations [13,14]. Active mechanical input in RCGs significantly enhances the spatial uniformity of the cavitation cloud and dramatically increases the radical yield per unit volume [15,16]. Extensive research has focused on optimizing RCG performance; for instance, Sun et al. [17] demonstrated that the arrangement of cavitation generating units (CGUs) directly influences energy efficiency, while Zhang et al. explored the synergy between radial length and installation positions to balance reaction intensity and fluid transport capacity [18]. Gostiša et al. even evaluated the removal rates of Chemical Oxygen Demand (COD), Total Organic Carbon (TOC) and Biochemical Oxygen Demand (BOD) in an 800 L pilot-scale reactor, confirming the engineering feasibility of the rotary approach [19]. Despite these advances, a fundamental challenge remains: the energy utilization efficiency of conventional RCGs is often limited by the simplicity of the tooth or disk geometry, and the complex synergistic mechanisms between shear-induced cavitation and vortex-induced cavitation are not yet fully understood. Table 1 fully covers the dimensions of geometric elements, energy input evaluation methods, and performance evaluation systems, to clearly define the incremental characteristics of this study. In terms of pit-type rotary cavitation devices, Badve et al. [20] utilized a rotor with distributed surface pits to treat wood-processing wastewater. Their work only adopted COD removal as the single evaluation index without quantitative cavitation efficiency calculation, and lacked systematic geometric optimization and flow field simulation, which cannot fully reflect the internal cavitation mechanism and overall treatment performance.

To bridge this gap, this study proposes a novel grooved-tooth rotary cavitation generator (GRCG). The core innovation lies in the strategic integration of micro-grooves on the rotor tooth surfaces, engineered to manipulate the local Reynolds number and induce high-frequency micro-vortexes. These grooves are hypothesized to intensify localized pressure oscillations and extend the residence time of cavitation bubbles in the high-shear region, thereby maximizing the oxidative yield. This investigation presents a multi-dimensional analysis of the proposed GRCG. Utilizing three-dimensional transient numerical simulations coupled with the SST k-ω turbulence model and the Zwart-Gerber-Belamri cavitation model, we systematically analyze the effects of critical parameters, the stator-rotor radial clearance L and rotational speed N on the evolution of the cavitation cloud, pressure pulsation characteristics, and vapor volume fraction.

Table 1: Systematic comparison of representative rotor-stator cavitation studies (2013–2026).

Reference	Year	Core Geometry Elements	Energy Evaluation Method	Performance Evaluation System	Core Limitations
Badve et al. [20]	2013	Pit-distributed rotor & matched stator	No quantitative energy efficiency indicator	Single COD removal index	Only prototype-scale test; no systematic optimization
Sun et al. [17]	2021	Straight cylindrical teeth, multi-ring arrangement	Cavitation energy efficiency (numerical)	Single disinfection performance	Cavitation only relies on inter-tooth shear, no vortex enhancement
Gostiša et al. [19]	2021	Pin-type protruding units on disk surface	Specific energy consumption per unit water volume	COD/TOC/BOD multi-index (pilot scale)	High processing cost, pins are easy to wear and clog
Zhang et al. [18]	2024	Straight teeth with variable radial length	Numerical cavitation energy efficiency	Pure numerical simulation	No experimental verification of actual treatment performance
This work	2026	Square teeth with micro-grooves on all four sides, staggered meshing	Dual indicators: cavitation energy efficiency + unit water treatment energy consumption	Three-dimensional cross-validation: transient CFD simulation + Rhodamine B degradation + *E. coli* inactivation	Bench-scale prototype, no same-platform horizontal comparison with other structures

A grooved-tooth rotor structure is proposed for the first time. By introducing micro-grooves on all four sides of the tooth, the synergistic effect of shear cavitation and vortex-induced cavitation is enhanced, which breaks the limitation that traditional straight-tooth structures rely solely on throttling shear to generate cavitation. A multi-dimensional validation system combining transient CFD (Computational Fluid Dynamics) numerical simulation, organic pollutant degradation (Rhodamine B) and microbial inactivation (*E. coli*) is established, making up for the deficiency of most existing studies that use a single evaluation index. The quantitative transmission chain of "structural parameter-operating parameter-cavitation intensity-pollutant removal efficiency" is constructed, providing a quantitative basis for the scale-up design of industrial rotary cavitation reactors.

2 Materials and Methods

2.1 Rotating Generators of Hydrodynamic Cavitation

The model of the new grooved-tooth rotary cavitation generator is shown in Fig. 1. It consists of a coaxially arranged rotor and stator, featuring an overall profile characterized by both conical and cylindrical elements. The rotor is equipped with square teeth containing grooves (hereinafter referred to as "rotor teeth"). Each rotor tooth is designed with groove structures on all four sides to enhance disturbance capabilities. Corresponding square teeth are arranged on the stator (hereinafter referred to as "stator teeth"). These two sets of teeth are configured in a staggered meshing layout, forming multiple fluid channels where shear action is predominant. This structure strengthens fluid disturbance through the shear effect between the rotor and stator teeth, thereby promoting bubble formation. The design of the groove structure further increases the flow path and local resistance of the fluid between the teeth, extending the fluid's residence time. During high-speed rotation, the fluid is subjected to intense, high-strength shear forces, increasing the probability of cavitation and improving the overall cavitation intensity and energy efficiency. The rotor and stator teeth are arranged uniformly in the axial direction, with the stator having one more ring of teeth than the rotor. The circumferential distribution angle of a single tooth is approximately 12.5°. Detailed structural dimensions and arrangement parameters are provided in Table 2.

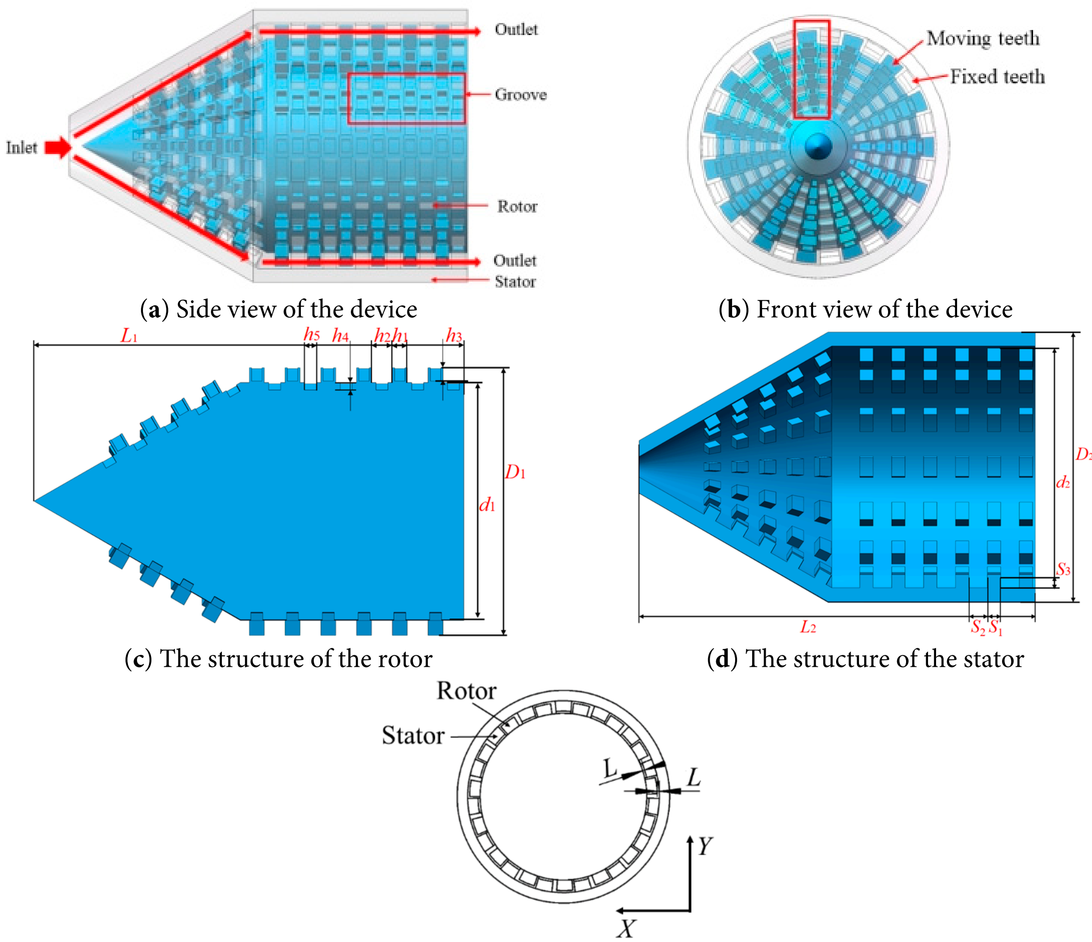

(**a**) Side view of the device
(**b**) Front view of the device
(**c**) The structure of the rotor
(**d**) The structure of the stator
(**e**) Schematic diagram of radial distance L between mover and stator clearance

Figure 1: Structural diagram of the rotating cavitation generator.

Table 2: Structural parameters of rotating cylinder and fixed cylinder.

Factors of Rotor	Values	Factors of Stator	Values
Rotor outer diameter D_1 (mm)	180	Stator outer diameter D_2 (mm)	204
Rotor inner diameter d_1 (mm)	160	Stator inner diameter d_2 (mm)	184
Total length of rotor L_1 (mm)	288	Stator total length L_2 (mm)	1216

Table 2: *Cont.*

Factors of Rotor	Values	Factors of Stator	Values
Tooth width h_1 (mm)	10	Tooth width S_1 (mm)	10
Axial distance h_2 (mm)	14	Axial distance S_2 (mm)	14
Tooth space depth h_3 (mm)	9	Tooth height S_3 (mm)	10
Groove tooth height h_4 (mm)	5	Number of teeth	15
Groove tooth width h_5 (mm)	8	Number of turns	11
Number of teeth	15	Number of moving teeth turns	10

The internal flow field of the grooved-tooth shear cavitation generator is numerically simulated using Ansys Fluent. Cavitation is a process of instantaneous phase transition within the liquid, and the Mixture model is used to simulate the separation of the vapor-liquid phases during cavitation. In this simulation, water at 25°C is used as the medium, with a saturation vapor pressure of 3540 Pa. The fluid inlet is set with a velocity inlet boundary condition, with an inlet velocity of 1 m/s, and the fluid outlet uses a pressure outlet boundary condition, with an outlet pressure equal to standard atmospheric pressure (101,325 Pa). In the solution algorithm, the velocity-pressure coupling algorithm is set to "Coupled," with the pressure discretization method chosen as PRESTO! and QUICK used for the discretization of momentum and volume fraction [21]. A second-order upwind scheme is employed for other physical quantities. To ensure accurate results, a sufficient number of iterations is assigned for each time step, with the total time step iterations and unit time step iterations set to 50 and 300, respectively. Polyhedral meshes with a minimum orthogonal quality of 0.09 were adopted for mesh generation in this work. The total vapor volume and vapor volume fraction were selected as quantitative criteria to conduct the mesh independence verification, and detailed data for five mesh schemes are summarized in Table 3. The results indicate that both the total vapor volume and vapor volume fraction gradually converge to stable values as the mesh number increases. Comparative analysis of five mesh resolutions (coarse, moderately coarse, medium, moderately fine, and fine) demonstrates that the medium mesh with 750,552 elements and 197,892 nodes is selected as the optimal discretization scheme for all numerical simulations of the cavitator model.

Table 3: Mesh sensitivity analysis.

Max Mesh Size (mm)	Number	Vapor Volume (mm^3)	Vapor Volume Fraction (%)
3	524,717	1,058,000	7.35
2.5	660,498	1,113,000	7.98
2	750,552	1,259,000	8.34
1.5	965,516	1,196,000	8.25
1	1,148,114	1,128,000	8.20

In the numerical calculations of the rotating cavitation generator, the governing equations mainly include the fundamental fluid dynamics equations, such as the continuity equation (mass conservation equation) and the momentum conservation equation (Navier-Stokes equation). These are typically combined with a cavitation model to describe the vapor-liquid phase transition process. Continuity Equation (Mass

Conservation Equation) is used to describe the mass conservation of the fluid, ensuring that the mass of the fluid within the cavitation generator is conserved. The equation is formulated as:

$$\frac{\partial_{\rho_m}}{\partial_t} + \nabla \cdot (\rho v_m) = 0 \tag{1}$$

$$\vec{v}_m = \frac{\sum_{k=1}^{n} \alpha_k \rho_k v_k}{\rho_m} \tag{2}$$

$$\rho_m = \sum_{k=1} \alpha_k \rho_k$$

$$\mu_m = \alpha_v \mu_v + (1 - \alpha_v) \mu_l \tag{3}$$

where μ_v is the vapor dynamic viscosity, μ_l is the liquid dynamic viscosity, and α_v is the vapor volume fraction.

Momentum Conservation Equation (Navier-Stokes Equation) is formulated as:

$$\frac{\partial}{\partial_t}(\rho_m v_m) + \nabla \cdot (\rho_m v_m v_m) = -\nabla P + \nabla \cdot \left[\mu_m \left(\nabla v_m + (\nabla v_m)^T\right)\right] + \vec{F} - \nabla \cdot \left(\rho_m \overline{u' u'}\right) \tag{4}$$

where ρ_m is the mixed density of the water phase and the bubble phase, v_m is the mass-averaged velocity, P is the static pressure, μ_m is the mixture molecular viscosity, $\vec{F}$ is the volumetric force (only includes gravitational acceleration, $\vec{F} = \rho_m \overline{g}$ all other volumetric forces are set to zero). The turbulent stress term arises from the averaged product of velocity fluctuations u'.

The turbulence model is used to simulate turbulent phenomena in numerical computations. Commonly used turbulence models for cavitating flows include Direct Numerical Simulation (DNS), Large Eddy Simulation (LES), and Reynolds-Averaged Navier-Stokes (RANS). Direct Numerical Simulation (DNS) resolves all turbulent scales ranging from large-scale flow vortices down to the smallest Kolmogorov microscales without any turbulence modeling. Although DNS can capture full details of small-scale turbulent structures with high fidelity, it imposes extremely high computational cost, as its computational load rises sharply with the 9/4 power of Reynolds number. For this reason, DNS is rarely adopted for industrial-scale cavitation flow simulations with high Reynolds numbers; however, it lacks detailed control of the small-scale turbulence. LES, while capable of calculating vortex structures, consumes excessive computational resources, leading to long simulation times, making it difficult to apply in practice. In contrast, three turbulence models in RANS are widely applicable, namely the standard k-ε model, the RNG k-ε model, and the Realizable k-ε model, all of which are designed for turbulence calculation in high Reynolds number flow fields. The RANS model simplifies the instantaneous fluctuations and unsteady phenomena in turbulence by averaging the flow field over time, primarily capturing the overall trend and large-scale flow characteristics. In the rotating hydrodynamic cavitation generator, local instabilities are induced by rotational flow and shear forces, but these instantaneous instabilities have minimal impact on the overall cavitation behavior. The RANS model effectively captures the formation and development of cavitation bubbles. Among these, the Realizable k-ε model improves upon the standard version by modifying the turbulence viscosity formula and the dissipation rate equation, significantly enhancing the prediction accuracy for flow separation, rotational effects, and highly curved flows [9,10]. The governing equations are as follows:

$$\frac{\vartheta(\rho k)}{\vartheta t} + \frac{\vartheta(\rho k u_i)}{\vartheta x_i} = \frac{\vartheta}{\vartheta x_j}\left[\left(u + \frac{u_t}{\sigma_k}\right)\frac{\vartheta k}{\vartheta x_j}\right] + P_k - \rho\varepsilon \tag{5}$$

The standard k-ε turbulence model contains two transport equations: one for turbulent kinetic energy k, and the other for turbulence dissipation rate ε. The turbulence dissipation rate ε characterizes the rate at which turbulent kinetic energy is converted into internal energy via viscous friction. The transport equation for the turbulence dissipation rate ε is:

$$\frac{\vartheta(\rho\varepsilon)}{\vartheta t} + \frac{\vartheta(\rho\varepsilon u_i)}{\vartheta x_i} = \frac{\vartheta}{\vartheta x_j}\left[\left(u + \frac{u_i}{\sigma_k}\right)\frac{\vartheta\varepsilon}{\vartheta x_j}\right] + \rho C_{1\varepsilon}\frac{\varepsilon}{k}P_k - \rho C_{2\varepsilon}\frac{\varepsilon^2}{k} \tag{6}$$

where ε represents the turbulence dissipation rate, empirical constants $C_{1\varepsilon}$ is 1.44, empirical constants $C_{2\varepsilon}$ is 1.92, σ_k is the turbulent Prandtl number 1.0 for the turbulence kinetic energy k, u is the molecular dynamic viscosity, N·s/m^2, u_t is the turbulent dynamic viscosity, N·s/m^2, P_k is the turbulence kinetic energy generated by velocity gradients, k is the turbulence kinetic energy, m^2/s^2, ρ is the density of the turbulent mixture, kg/m^3.

The turbulent Reynolds stress and the calculation formula of turbulent eddy viscosity are:

$$\mu_t = \rho_m C_\mu \frac{k^2}{\varepsilon} \tag{7}$$

$$-\rho_m \overline{u_i' u_j'} = \mu_t\left(\frac{\partial u_i}{\partial x_j} + \frac{\partial u_j}{\partial x_i}\right) - \frac{2}{3}\rho_m k\delta_{ij} \tag{8}$$

The cavitation initiation mechanism in the rotating cavitation generator is primarily divided into two parts. The first is cavitation caused by centrifugal force. When the rotor rotates at high speed, the fluid is subjected to inertial centrifugal forces. The liquid tends to move toward the outer part of the groove, causing a pressure drop at the bottom of the groove, where the pressure decreases to below atmospheric pressure. As the outward velocity of the fluid increases, the pressure differential enlarges, ultimately generating a differential force on the liquid that drives the fluid inward, thereby triggering cavitation. The second mechanism involves vortex cavitation caused by mechanical shear forces based on Bernoulli's equation. When the fluid passes through the throttling region, the flow velocity increases, resulting in a pressure drop that generates cavitation. During the rotor's rotation, the presence of fixed teeth causes a sudden reduction in the flow area, thereby creating a throttling effect. The throttled fluid then flows into the rotor groove, where the fluid is released, pressure is restored, and the cavitation bubbles collapse. The cavitation model used in this study is the Zwart-Gerber-Belamri model based on the Rayleigh-Plesset equation. This model is widely recommended due to its fast convergence speed and high accuracy. It has been used to analyze the cavitating flow process inside reactors [22,23]. The numerical simulation method adopted in this study has been widely validated in cavitation flow analysis of rotary fluid machinery [24]. The Zwart-Gerber-Belamri equation is:

$$\frac{\partial(\alpha_v\rho_v)}{\partial t} + \frac{\partial(\alpha_v\rho_v u_i)}{\partial x_i} = \dot{m}^+ + \dot{m}^- \tag{9}$$

$$\dot{m}^- = C_{\text{vap}} \frac{3\alpha_{\text{nuc}} p_v (1-\alpha_{\text{v}})}{R_B} \sqrt{\frac{2}{3} \frac{(p_v(T_\infty) - p)}{\rho_l}} \tag{10}$$

$$\dot{m}^+ = C_{cond} \frac{3\alpha_v \rho_v}{R_B} \sqrt{\frac{2}{3} \frac{(p - p_v(T_\infty)}{\rho_l}} p > p_v(T_\infty) \tag{11}$$

where $\dot{m}^+$ and $\dot{m}^-$ represent the source terms for mass exchange between the gas and liquid phases per unit time, referred to as the vaporization term and condensation term, respectively. C_{vap} is the condensation coefficient, approximately 0.01, C_{cond} is the evaporation coefficient, approximately 50, α_{nuc} is the cavitation nuclei volume fraction, approximately 5×10^{-4}, α_{v} is the vapor phase volume fraction, ρ_l is the liquid phase density, ρ_v is vapor phase density, R_B is the radius of a single cavitation bubble, p_v is the micro-liquid saturation vapor pressure, Pa, p is the flow field pressure, Pa.

2.2 Experimental Apparatus

The performance verification experiments for the novel grooved-tooth rotary cavitation generator were conducted in a closed-loop water circulation system. A schematic of the overall experimental apparatus is illustrated in Fig. 2. In this system, the cavitation generator is driven by a 1.5 kW, 380 V three-phase asynchronous motor. A WB620 vector frequency inverter was utilized for speed control, thereby facilitating the circulation of the fluid. During the experimental procedure, the motor speed was increased incrementally from low-load conditions until the target rotational speed was reached and a stable operating state was maintained.

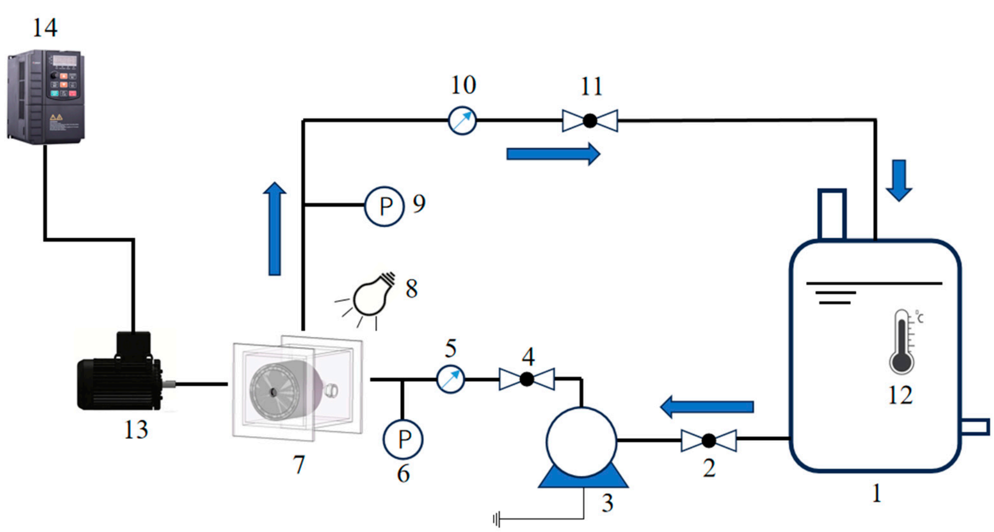

Figure 2: Schematic diagram of experimental device. (1. Water tank; 2. Ball valve; 3. Centrifugal pump; 4. Ball valve; 5. Electromagnetic flowmeter; 6. Pressure sensor; 7. Novel grooved-tooth rotational cavitation generator; 8. LED light; 9. Pressure sensor; 10. Electromagnetic flowmeter; 11. Ball valve; 12. Thermometer; 13. Motor; 14. Frequency converter).

As illustrated in Fig. 3, prior to starting the experiment, ball valves 1 and 11 must be closed, and the water tank must be filled to a volume of 30 L to ensure system safety and measurement accuracy. Subsequently, ball valves 2 and 11 are opened, and the inlet velocity is regulated by adjusting ball valve

4. The rotational speed of the motor is controlled via the WB620 vector frequency inverter 14. To collect pressure data, pressure sensors 6 and 9 are installed at the inlet and outlet, respectively, with a measurement accuracy of ±0.4%. Driven by the centrifugal pump 3, the solution enters the novel grooved-tooth rotary cavitation generator 7. Under the synergistic action of the rotor and stator, the fluid completes the circulation process and finally flows back into the water tank 1.

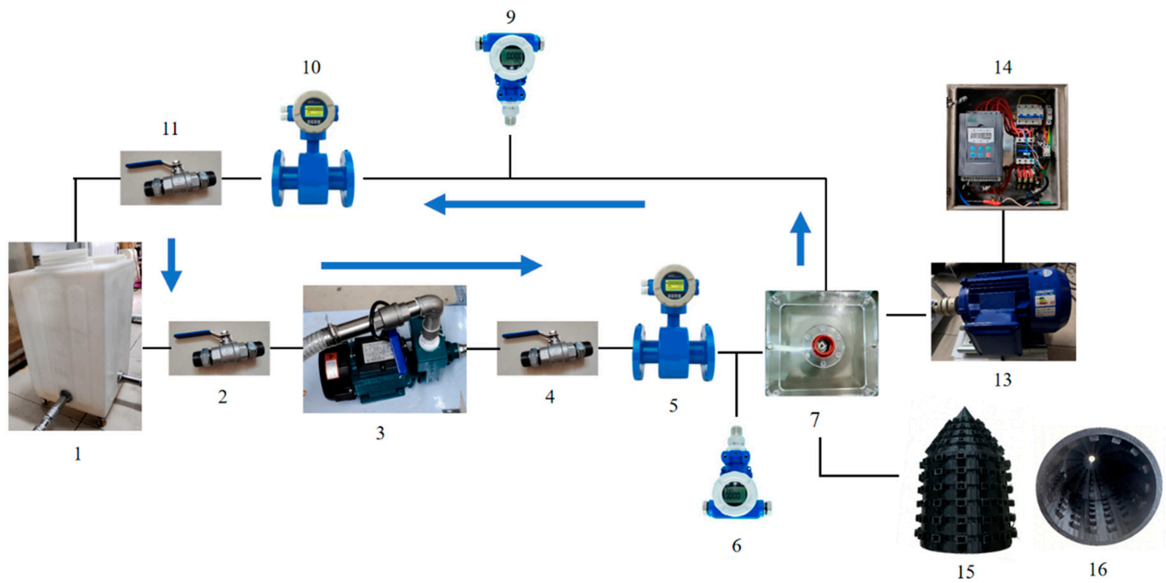

Figure 3: Physical diagram of experimental device.

2.3 Experimental Design

In this study, Escherichia coli (*E. coli*) and Rhodamine B were selected as the biological indicator and representative organic pollutant, respectively, to comprehensively evaluate the disinfection and degradation performance of the new grooved-tooth rotary cavitation generator. The experiments were conducted in a controlled environment at 25°C, using 15 L of sterilized experimental water for each test group.

For the *E. coli* inactivation experiments, a 20 mL bacterial suspension was prepared under sterile conditions and uniformly mixed into the water tank. The system underwent a 10-min pre-circulation at a low speed of 600 r/min to eliminate concentration gradients and air bubbles. Subsequently, the generator operated at a stable speed of 3500 r/min, with 20 mL samples collected from the outlet at intervals of 0, 10, 20, and 30 min. The collected samples were subjected to gradient dilution and inoculated onto LB (Lysogeny Broth) agar plates, followed by incubation at 37°C for 48 h. The bacterial concentration C (CFU/mL) in the water samples was calculated using the following formula:

$$C = \frac{N \times M}{V} \tag{12}$$

where N is the number of effective colonies on the plate, M is the dilution factor, and V is the inoculation volume, mL.

For the Rhodamine B degradation experiments, a precisely weighed amount of Rhodamine B solid was dissolved in 15 L of water. After a 10-min pre-circulation at 500 r/min, an initial sample was collected. During the formal experiment, the rotation speed (up to 3500 r/min) and inlet flow rate were adjusted according to the preset parameters. Samples were collected from the water tank at 20, 40, 60, and 80 min.

The absorbance–concentration standard curve of Rhodamine B solution was measured by ultraviolet spectrophotometer, and the fitted standard curve equation is as follows:

$$Y_{RhB} = 0.25575C_{RhB} + 0.0587 \tag{13}$$

where Y_{RhB} represents the absorbance value, and C_{RhB} denotes the mass concentration of Rhodamine B solution.

The absorbance of the retained Rhodamine B solution samples was measured to obtain the solution concentration, and the degradation rate was further calculated. The degradation rate calculation formula is given as follows:

$$\frac{C_{RhB0} - C_{RhB1}}{C_{RhB0}} \times 100\% = \frac{Y_{RhB0} - Y_{RhB1}}{0.25575C_{RhB0}} \times 100\% \tag{14}$$

3 Results and Discussion

3.1 Transient Evolution of the Cavitating Flow Field inside the Cavitation Generator

Given that the core operating principle of a rotating cavitation generator lies in the relative motion between the rotor and the stator, the radial gap distance between the rotor and stator, as well as the flow-field variation inside the grooves, directly determines the cavitation effect. To investigate the evolution characteristics of bubbles in the radial direction between the rotor and stator, this study selects cross-section a of the novel grooved-tooth rotating cavitation generator as the analysis object, as shown in Fig. 4.

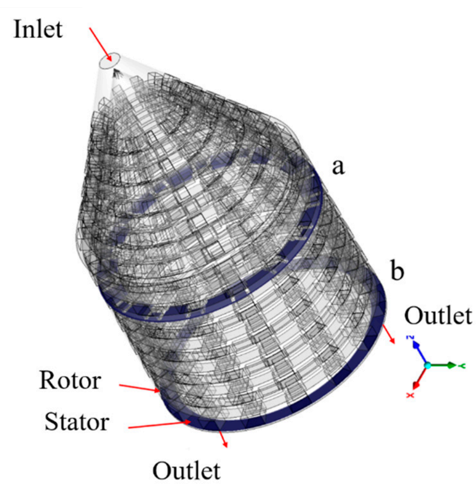

Figure 4: 3D diagram of a novel grooved-tooth rotating cavitation generator.

The simulation captured the flow-field characteristics of the cavitation generator from the initial start-up stage to the quasi-steady operating stage under the conditions of a 2 mm radial gap between the rotor and stator and a rotational speed of 3500 r/min. Three representative moments were selected, T = 0.01 s (start-up acceleration stage), T = 0.02 s (transition stage), and T = 0.03 s (quasi-steady stage), with emphasis on analyzing the evolution of the gas-phase volume fraction, static pressure distribution, velocity vectors, and turbulent kinetic energy on cross-section a, as shown in Fig. 5.

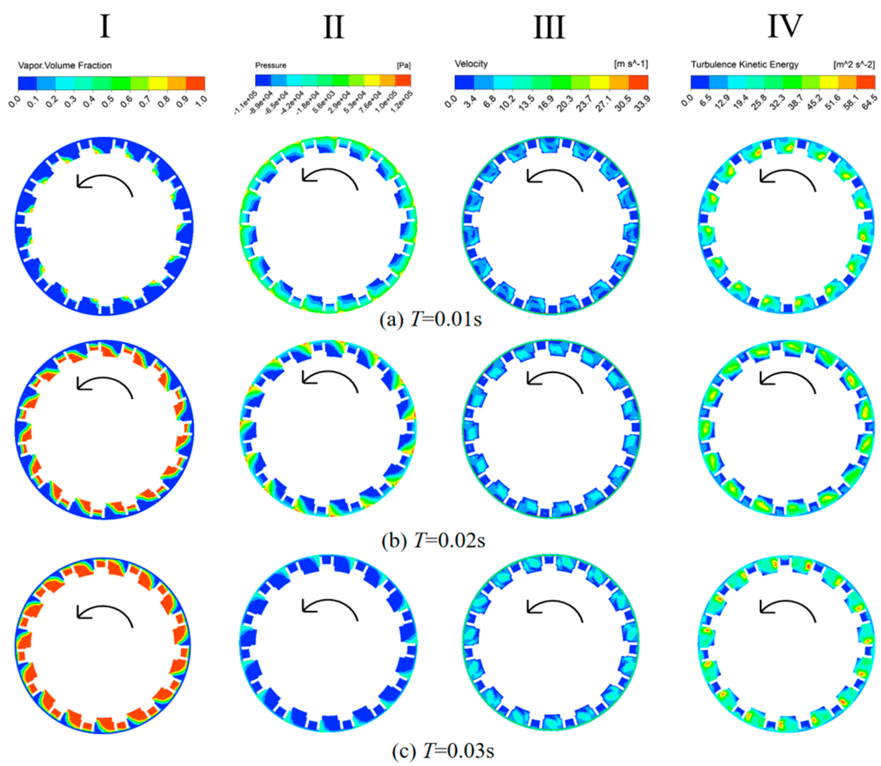

Figure 5: Cavitation characteristics of the flow field at T = 0.01 s, T = 0.02 s and T = 0.03 s ((**I**): Gas Phase Volume Fraction Contour, (**II**): Pressure distribution map, (**III**): Velocity vector map, (**IV**): Turbulent kinetic energy distribution map).

Although local pressure reduction occurs on the suction side of the rotor teeth, the gas-phase volume fraction remains nearly zero, indicating that the cavitation threshold has not yet been reached. At T = 0.02 s, the increasing rotational speed enhances the shear interaction between the rotor and stator. A distinct low-pressure region appears on the suction side of the rotor teeth, leading to cavitation inception. Sheet cavitation is observed along the inner wall of the grooves. Meanwhile, boundary-layer separation and local vortices are induced near the groove edges, causing the turbulent kinetic energy to increase from 6.5 to 12.9 m^2/s^2. This indicates a significant enhancement of flow shear and turbulence intensity. At T = 0.03 s, the low-pressure region further expands and covers most of the groove interior and part of the radial clearance. The vapor distribution becomes more uniform, and the initially separated sheet cavitation regions merge into a relatively stable cavitation cloud inside the grooves. The regions with high turbulent kinetic energy are spatially consistent with those of high gas-phase volume fraction, demonstrating that cavitation evolution significantly strengthens turbulent fluctuations in the rotor–stator interaction region.

The fluid flows into the cavitation generator through the central inlet, undergoes shear induced by the interaction between the rotor and stator, and is then discharged through the axial outlet. To capture the spatial details of cavitation phase-change inception and cavity morphology evolution more precisely, the axial characteristic line from cross-section a to cross-section b in Fig. 4, which includes the rotor–stator interaction region, was selected as the observation object. The streamwise distributions of gas-phase volume fraction, static pressure, velocity, and turbulence intensity are shown in Fig. 6.

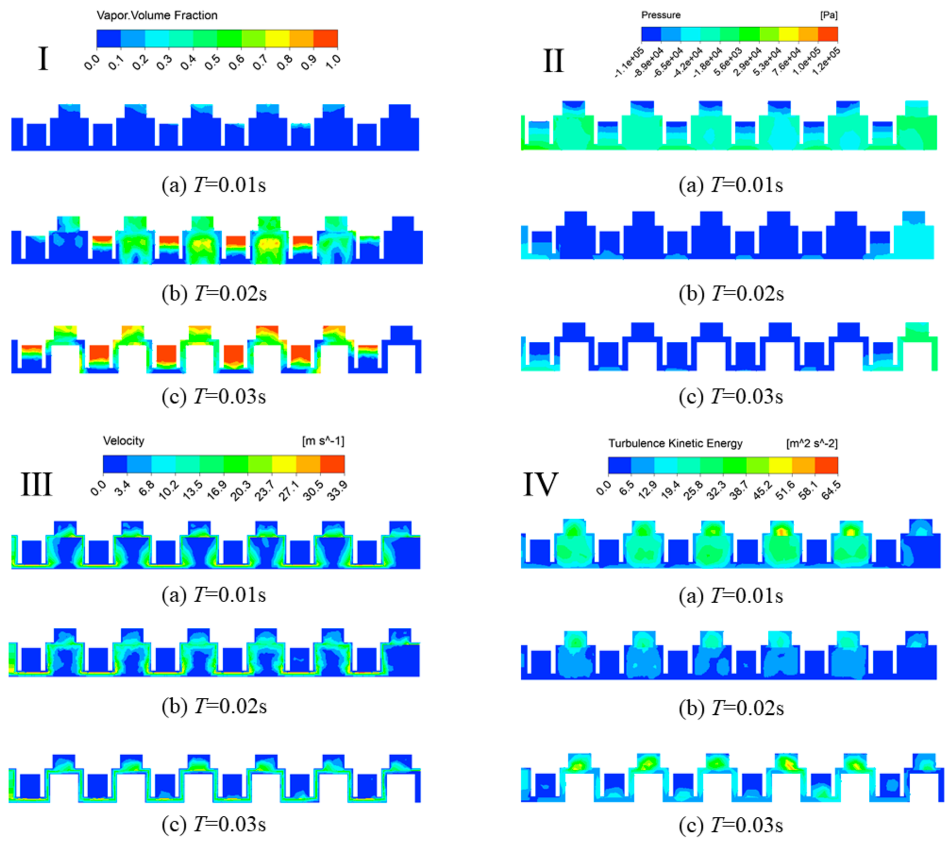

Figure 6: Cavitation characteristics of axial flow field at T = 0.01 s, T = 0.02 s and T = 0.03 s ((**I**): Volume distribution cloud chart of gas phase, (**II**): Pressure distribution chart, (**III**): Velocity vector chart, (**IV**): Turbulent kinetic energy distribution chart).

Fig. 6 presents the temporal evolution of cavitation characteristics in the axial flow field from cross-section a to cross-section b during 0.01–0.03 s. At T = 0.01 s, the flow passage is mainly occupied by the liquid phase, with only small vapor regions appearing near several corners, indicating incipient cavitation. The pressure field remains relatively uniform, and both the velocity and turbulent kinetic energy are low, suggesting a stable flow state with weak disturbances.

As the time increases to T = 0.02 s, the vapor regions expand noticeably, especially near the corners and narrow regions of the flow passage. This is accompanied by the enlargement of local low-pressure zones and the appearance of high-velocity regions, indicating the further development of cavitation. Meanwhile, the turbulent kinetic energy becomes more uneven and increases near the bubble front and flow-passage bends, reflecting enhanced flow instability.

At T = 0.03 s, the vapor phase further spreads along the inner wall of the passage, and the local gas-phase volume fraction approaches 1, indicating that cavitation has nearly reached a saturated state. The low-pressure region becomes more pronounced, while alternating high-speed flow and recirculation zones lead to strong local turbulence. The peak turbulent kinetic energy reaches 64.5 m^2/s^2, confirming that cavitation evolution induced by the groove structure significantly enhances turbulent fluctuations and becomes an important mechanism of flow-field energy dissipation.

To further investigate the combined effects of vorticity, flow velocity, and pressure on cavitation in the flow field, three iso-surface distributions shown in Fig. 7 were presented in this study. These include the iso-surfaces of gas-phase volume fraction with vorticity, static pressure with gas-phase volume fraction, and gas-phase volume fraction with turbulent kinetic energy. Based on these results, the interactions among these physical quantities were systematically analyzed.

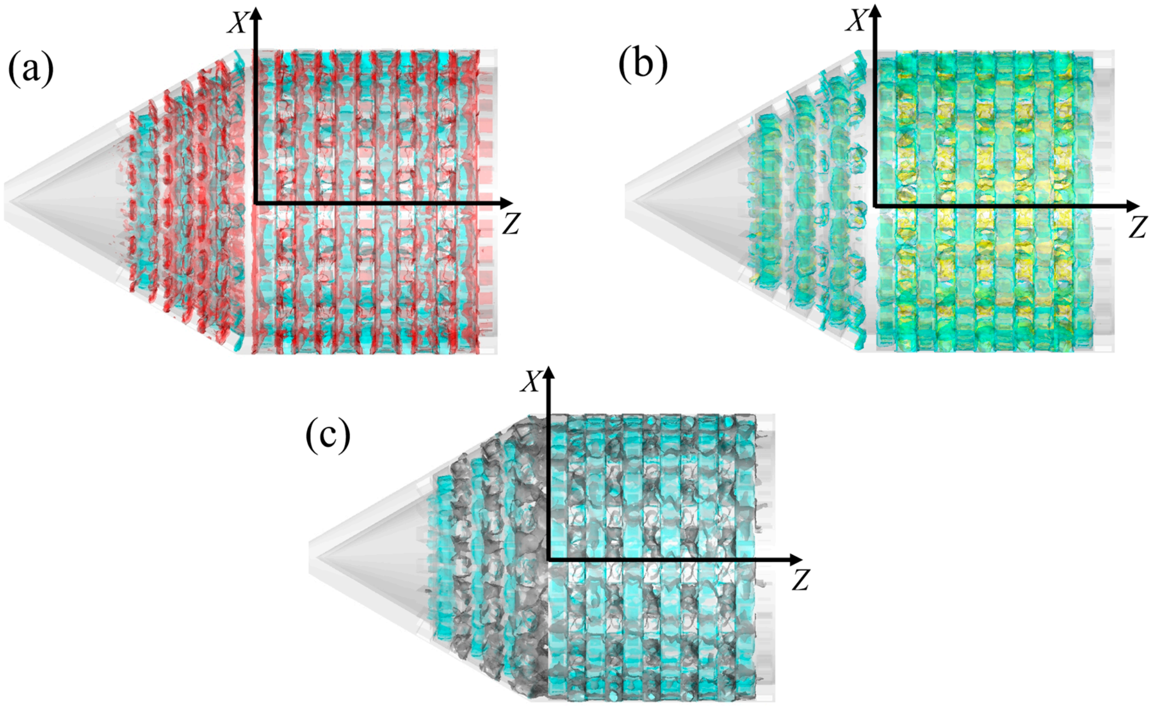

Figure 7: (**a**) Contour surface distributions of vapor phase (blue) and vorticity (red); (**b**) contour surface distributions of pressure (yellow) and vapor phase (blue); and (**c**) contour surface distributions of vapor phase (blue) and turbulent kinetic energy (gray).

Fig. 7a shows the surface distributions of gas-phase volume fraction (blue) and vorticity (red). The gas-phase volume fraction reflects the formation of cavitation bubbles in the fluid, with the blue regions representing the areas where cavitation bubbles are present. Vorticity represents the intensity of fluid rotation, and the red regions indicate areas with strong vortical motion. It can be observed that the high-vorticity regions overlap with the regions of high gas-phase volume fraction, indicating that local rotation and flow disturbances in these vortical regions may promote the formation and development of cavitation bubbles. In Fig. 7b, the low-pressure regions (yellow) are closely associated with the regions of high gas-phase volume fraction (blue). The low-pressure environment provides favorable conditions for cavitation inception. When the local pressure falls below the saturated vapor pressure of the liquid, the liquid changes into vapor, resulting in the formation of cavitation bubbles. Fig. 7c presents the distributions of turbulent kinetic energy (gray) and gas-phase volume fraction. An increase in turbulent kinetic energy generally enhances flow instability, thereby further promoting the generation and expansion of cavitation bubbles. The overlap between regions of high turbulence intensity and high gas-phase volume fraction indicates that turbulence accelerates the development of cavitation by intensifying flow disturbances.

Overall, the low-pressure regions provide the necessary conditions for bubble formation, while enhanced vorticity and turbulent kinetic energy accelerate cavitation development through local flow instability. The interaction among these four physical quantities jointly drives the occurrence and evolution of cavitation.

To investigate the internal flow characteristics of the cavitation generator and their influence on cavitation behavior, Fig. 8 presents the local flow features associated with cavitation generation in the rotor groove region. Particular attention is paid to the pressure distribution between the suction surface and the high-pressure region, as well as its effect on cavitation. The suction surface refers to the region on the rotor surface where the fluid velocity is relatively high and the pressure is relatively low; cavitation bubbles are generally generated in such low-pressure regions. By analyzing local pressure variations, the influence of flow characteristics on the development of cavitation behavior can be further clarified.

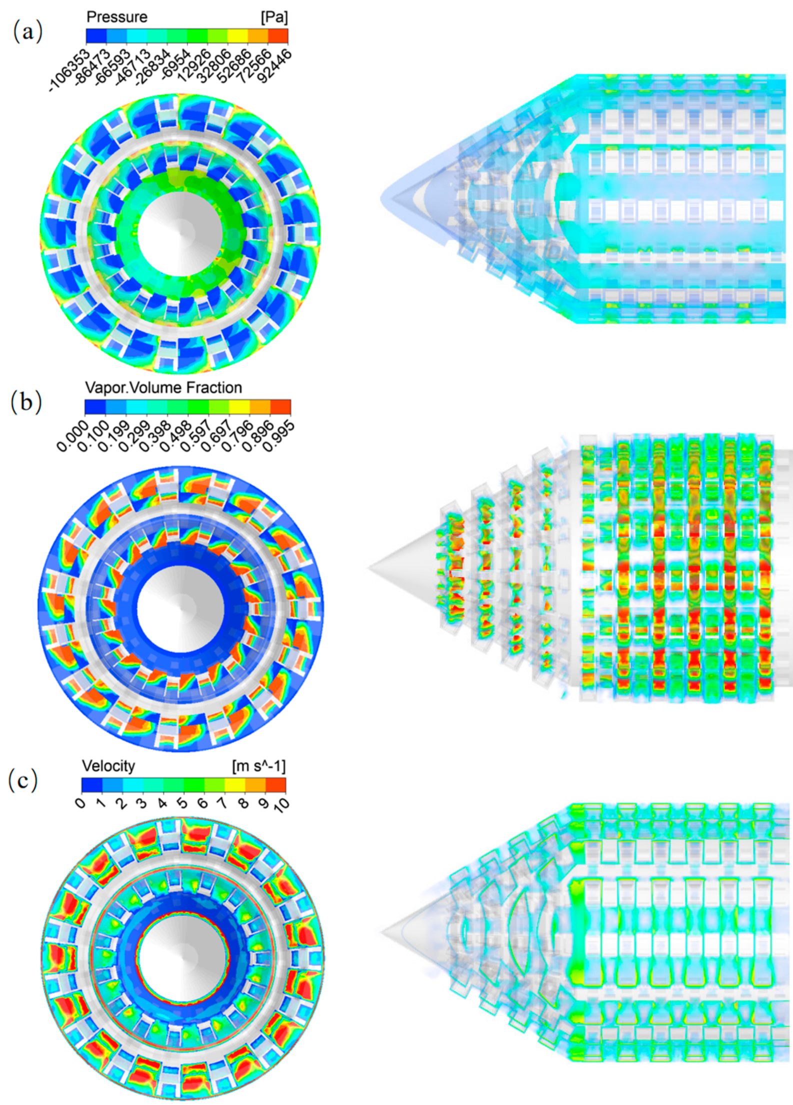

Figure 8: Generation of cavitation inside the groove ((**a**): Gas phase volume fraction distribution, (**b**): Pressure distribution, (**c**): Velocity vector diagram).

As shown in Fig. 8, during rotor rotation, the water flow in the groove region is driven by centrifugal force, resulting in distinct local high-pressure and low-pressure regions. The low-pressure region is mainly distributed near the suction side of the groove, where the gas-phase volume fraction increases significantly, indicating favorable conditions for cavitation inception. In contrast, the high-pressure region corresponds to weaker cavitation intensity and exhibits a suppressing effect on bubble generation. The groove distribution also shows a certain degree of flow continuity and regional transition between adjacent grooves. The spatial variation of the local pressure gradient affects the formation range and stability of the low-pressure region. Therefore, the groove shape and spacing play a key role in regulating the local pressure field. Rational optimization of the groove design can help expand the coverage of low-pressure regions and enhance the cavitation effect, providing a theoretical basis for structural improvement of the cavitation generator.

To investigate the dynamic evolution of the flow-field structure during the variation of rotational speed, Fig. 9 compares the velocity vector distributions at different rotation times, namely 0.01 s, 0.02 s, and 0.03 s. The results reveal the development of the fluid motion from an initially disordered state to an ordered rotational flow under the action of shear.

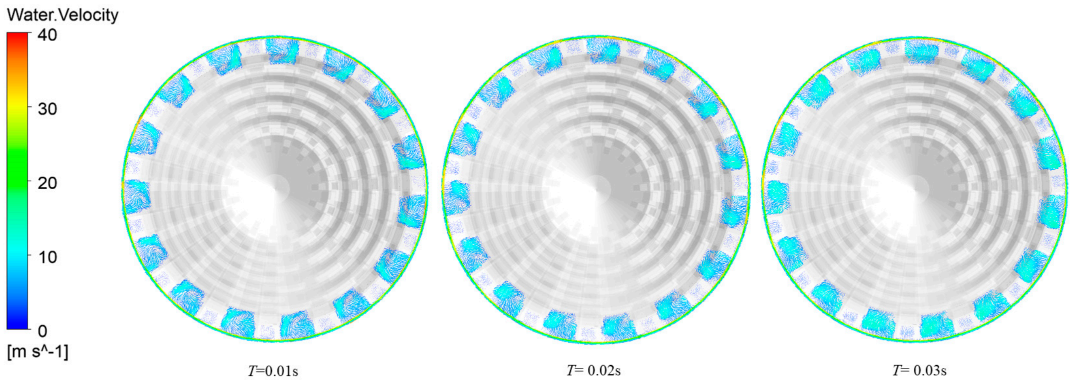

Figure 9: Velocity vector contours at different times.

As can be seen from the velocity vector contours in Fig. 9, the velocity vectors in the flow field gradually become more ordered as the rotation time increases. At 0.01 s, the velocity vector field exhibits obvious unsteady and disordered characteristics, with vector directions distributed irregularly in the radial flow passage. This indicates that the fluid motion is only weakly constrained by shear at this stage, and the flow field is still in the initial stage, where the fluid motion is not yet fully dominated by the rotational effect. At 0.02 s, the velocity vector distribution begins to become more organized. The fluid motion is increasingly affected by shear forces, and vortical flow starts to form inside the grooves. By 0.03 s, the flow field gradually reaches a stable state, and the consistency of the velocity direction throughout the domain is significantly enhanced, forming a typical rotating flow-field topology.

These results indicate that the flow field inside the rotating hydrodynamic cavitation generator gradually stabilizes over time. During this stabilization process, the rotor–stator shear interaction and centrifugal effect jointly promote the formation of a stable rotating flow pattern, which has a positive effect on the generation and development of cavitation bubbles. Such a stable rotating flow field is favorable for maintaining and expanding the cavitation region in space.

3.2 Flow Field and Cavitation Characteristics Analysis in the Rotor Region

To investigate how the radial clearance between the rotor and stator affects cavitation performance, simulation analyses were conducted by varying the radial gap distance. This study selected four typical clearance parameters (L = 1 mm, 1.5 mm, 2 mm, 2.5 mm). At a rotational speed of 4500 r/min and a duration of 0.03 s, the trends for gas phase volume (V_{vapor}), total gas phase volume (V_{total}), gas phase volume fraction (α), torque (T), power (P), and cavitation energy efficiency (η) were recorded. The resulting data are presented in Table 4.

Table 4: Effect of different radial distances of mover-stator clearance on cavitation performance of the cavitator.

Factors	Values	V_{vapor} (mm^3)	V_{total} (mm^3)	α (%)	T (N·m)	P (kW)	η (mm^3/kW)
L (mm)	1	349.03	1352.65	25.8	0.51	0.187	1866.47
	1.5	263.50	1352.65	19.48	0.55	0.202	1304.46
	2	256.49	1352.65	18.96	0.58	0.213	1204.19
	2.5	111.90	1352.65	8.27	0.62	0.227	429.95

Cavitation energy efficiency (n) and cavitation power (P) are used to evaluate the cavitation performance of the rotating hydrodynamic cavitation generator under different operating conditions in terms of both energy and spatial aspects. The cavitation rate is the ratio of the total cavitation bubble volume to the computational domain volume, and it characterizes the efficiency of cavitation generation in the spatial aspect, as shown in Eq. (15):

$$\alpha = \frac{V_{vapor}}{V_{total}} \tag{15}$$

where α is the cavitation rate, V_{vapor} is the total cavitation bubble volume in the computational domain, m^3, V_{total} is the total volume of the computational domain, m^3.

Torque and rotor speed are used to calculate the input power, as shown in Eq. (16):

$$P = \frac{n \times T}{9550} \tag{16}$$

where P is the input power, kW, n is the torque, n/m, T is the rotor speed, r/min.

Cavitation energy efficiency (n) is the ratio of the total vapor volume to the input power, and it characterizes the efficiency of cavitation generation in terms of energy, as shown in Eq. (17):

$$\eta = \frac{V_{vapor}}{P} \tag{17}$$

where η is the cavitation energy efficiency, mm^3/kW.

As the radial clearance between the rotor and stator increases, the cavitation performance indicators of the generator exhibit a significant downward trend. At a parameter setting of L = 1 mm, the total gas phase volume reaches 349.03 with a gas volume fraction of 25.8%, representing the maximum values within this structural parameter series. In contrast, when the radial clearance is increased to 2.5 mm, the total gas volume and volume fraction drop to 111.9 mm^3 and 8.27%.

This degradation occurs because the increase in radial clearance weakens the shear intensity between the rotor and stator, causing the high turbulent kinetic energy regions to retreat toward the center of the flow channel. The data suggest that the diminished shear effect weakens the stripping action on gaseous nuclei, thereby restricting bubble development. While the system torque (T) and input power (P) show a slight upward trend as the clearance widens, the cavitation energy efficiency (η) drops sharply—decreasing from 1866.47 mm^3/kW to 429.95 mm^3/kW, a reduction of nearly 77%. This indicates that under larger clearances, the cavitation volume generated per unit of energy consumption decreases drastically, leading to a significant decline in the device's energy conversion efficiency.

To visually evaluate the impact of the radial clearance L on the cavitation zone, the flow field models of the cavitation generator were compared for L values of 1 mm, 1.5 mm, 2 mm, and 2.5 mm. By extracting gas phase volume fraction cloud maps under different radial clearances, the spatial evolution of the cavitation was quantitatively analyzed. The global and local cloud maps are presented in Figs. 10 and 11.

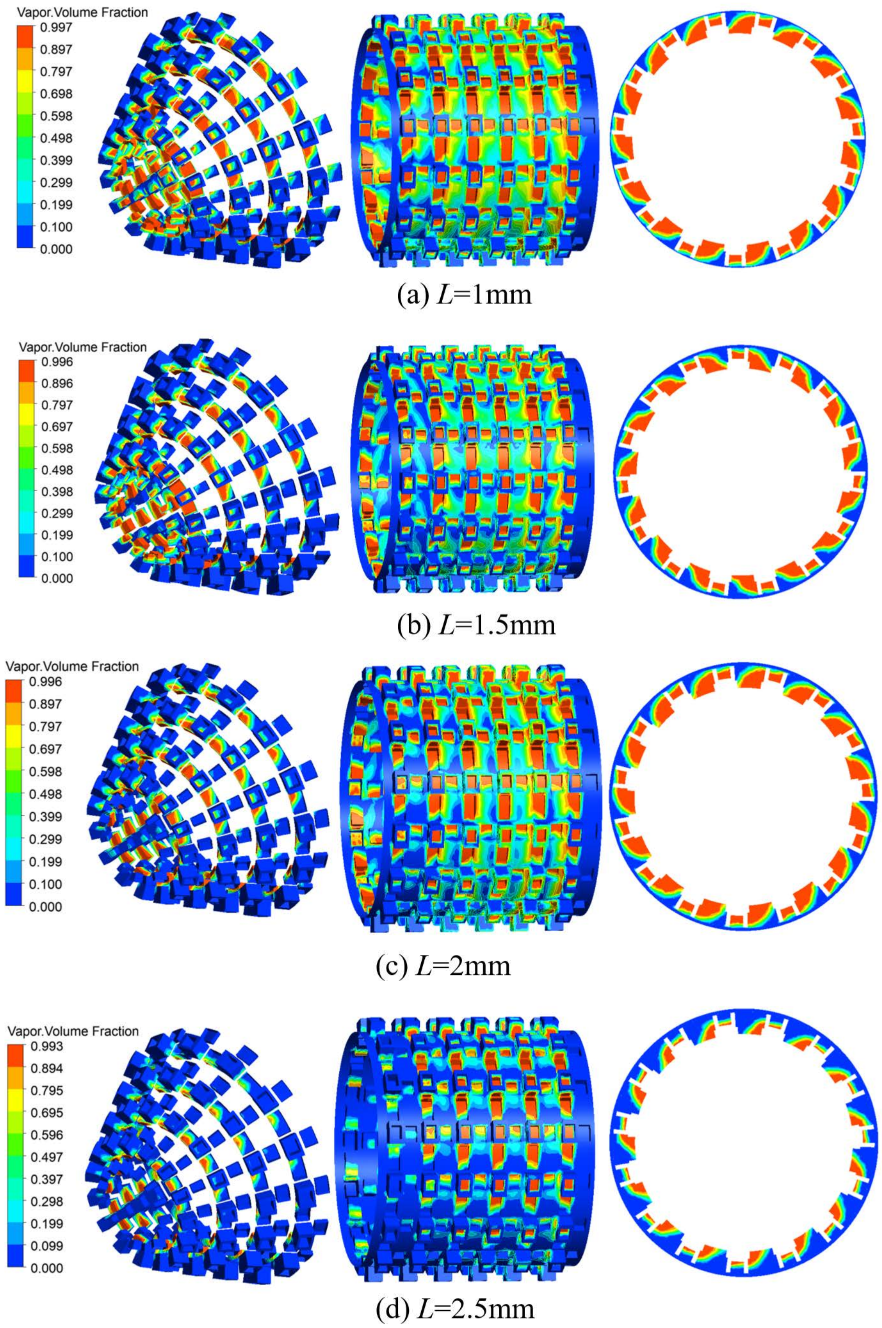

Figure 10: Gas phase volume contours of the mover at different radial gaps between the mover and stator.

As shown in Fig. 10, the gas phase is primarily distributed along the edges of the grooves on the rotor surface and within the shear zones between the rotor and stator, exhibiting a circumferential periodic distribution consistent with the tooth geometry. As the radial clearance L increases, the gas phase distribution initially shows good connectivity, forming distinct band-like structures. The large areas of red and orange in the cloud maps indicate high local gas content, where cavitation development is most intense. At L = 1.5 mm, the gas phase region remains prominent; however, compared to L = 1 mm, the continuity decreases, with high-concentration regions in certain grooves becoming intermittent and the overall coverage area slightly reduced.

As the radial clearance L further increases to 2 mm and 2.5 mm, the high-concentration gas phase regions shrink rapidly, evolving from continuous bands into discrete strips or spot-like distributions. At L = 2.5 mm, the gas phase is only sporadically distributed on a few tooth tips and their leeward sides, making it difficult to form a continuous gas band along the circumference.

To further quantify the impact of clearance size on cavitation yield, the total gas phase volume and gas volume fraction within the flow field were calculated, as shown in Fig. 11. The total gas phase volume exhibits a step-like decline as the clearance increases. At L = 1 mm, the total gas phase volume reaches as high as 349.03 mm^3, whereas at L = 2.5 mm, this value decreases to 111.9 mm^3, representing a reduction of approximately 68%. This indicates that even minor increments in clearance can cause a significant attenuation in total cavitation yield.

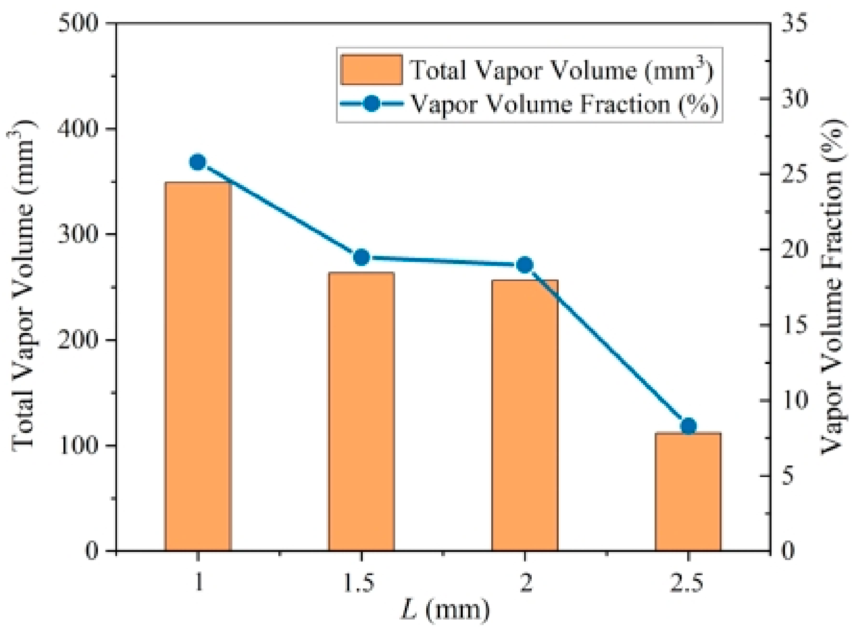

Figure 11: Diagram of rotor gas phase volume and gas phase volume fraction.

Consequently, within this series of structural parameters, a smaller radial clearance facilitates the formation of gas phase regions on the rotor surface and promotes a more uniform distribution. Conversely, as the radial clearance increases, the gas phase regions gradually shrink and tend toward discretization. This phenomenon demonstrates that variations in the radial clearance between the rotor and stator significantly alter both the formation range and the spatial distribution of the gas phase regions within the cavitation generator.

To quantitatively evaluate the regulatory effect of rotor speed on the performance of the rotary cavitation generator, numerical simulations were conducted under a constant inlet pressure of 0.1 MPa and a radial clearance L = 1.5 mm. Four typical rotational speeds—3000 r/min, 3500 r/min, 4000 r/min, and 4500 r/min—were selected to investigate the variation laws of key performance indicators, including: gas phase volume (V_{vapor}), total gas phase volume (V_{total}), gas phase volume fraction (α), torque (T), power (P), and cavitation energy efficiency (η). The relevant data are summarized in Table 5.

Table 5: Influence of different rotational speeds on the cavitation performance within the rotational hydrodynamic cavitation generator.

Factors	Values	V_{vapor} (mm^3)	V_{total} (mm^3)	α (%)	T (N·m)	P (kW)	η (mm^3/kW)
N (r/min)	3000	65.25	1352.65	4.8	0.49	0.154	423.70
	3500	167.13	1352.65	12.35	0.55	0.202	827.38
	4000	263.50	1352.65	19.48	0.60	0.251	1049.8
	4500	342.68	1352.65	25.33	0.64	0.301	1134.7

The simulation results indicate that as the rotational speed increases, the cavitation effect within the device exhibits a significant non-linear enhancement trend. The total gas volume V_{vapor} rises from 65.25 mm^3 at 3000 r/min to 342.68 mm^3 at 4500 r/min, an increase of over 425%. This demonstrates that the strong shear rates and high centrifugal force fields generated by high speeds effectively intensify turbulent fluctuations within the fluid, greatly promoting the expansion of low-pressure core regions and the explosive activation of cavitation nuclei.

Concurrently, the gas volume fraction increases from 4.8% to 25.33%, indicating a continuous expansion of the bubble volume distribution within the computational domain and a substantial rise in cavitation intensity. Regarding dynamic characteristics, as the speed increases, the torque T increases from 0.49 N·m to 0.64 N·m, and the power P rises from 0.154 kW to 0.301 kW, reflecting an increase in system energy input. However, this growth in energy input is far lower than the growth in gas phase volume. Consequently, the cavitation energy efficiency η improves significantly, rising from 423.7 mm^3/kW to 1134.7 mm^3/kW—an increase of 167.80%. This reflects a marked enhancement in the bubble generation capacity per unit of energy driven, signaling a simultaneous improvement in the system's energy efficiency level.

Therefore, increasing the rotational speed is an effective approach to enhancing the performance of rotary cavitation generators. Higher speeds accelerate bubble generation and increase cavitation intensity within the flow field, leading to improvements in both cavitation yield and overall system energy efficiency. This conclusion validates the feasibility of optimizing and controlling cavitation performance through speed adjustment, providing a theoretical foundation for practical industrial applications and operational matching of the device. Consequently, regulating rotational speed can serve as a primary means for the precise control of rotary cavitation generator performance, offering broad prospects for engineering applications.

As illustrated in Figs. 12 and 13, the rotor speed exerts a significant influence on the spatial distribution characteristics of the cavities within the generator. With the increase in speed, the gas phase distribution evolves from localized inception to global connectivity. To reveal the impact of speed parameters on the generation and transport processes of cavitation bubbles, numerical simulation studies were conducted at four typical rotational speeds: N = 3000 r/min, 3500 r/min, 4000 r/min, and 4500 r/min.

Fig. 12 illustrates the gas phase volume fraction contours inside the cavitation generator at various rotational speeds, while Fig. 13 presents the corresponding variation curves for gas phase volume and volume fraction. Based on the analysis of the contours and data curves, the influence of rotational speed on cavitation performance is highly significant.

At the lower speed of N = 3000 r/min, the low linear velocity at the tips of the rotor teeth results in minimal shear action. Consequently, the gas phase is primarily concentrated at the leading edges of the rotor teeth and localized within the gaps; the total gas volume is only 65.25 mm^3 with a volume fraction of 4.8%, indicating a small and sparsely distributed cavitation zone. As the rotational speed increases, the shear intensity within the flow field gradually intensifies. As seen in Fig. 12, the gas phase regions expand significantly, spreading aggressively toward the rotor-stator gaps and deep into the grooves, evolving from initial discrete spots into interconnected sheet-like cavity structures. The corresponding data show a clear growth trend in gas volume with increasing speed. Cavitation is most intense when the speed reaches 4500 r/min. High-concentration gas regions (indicated in red) occupy nearly the entire rotor-stator coupling zone, with the total gas volume reaching 342.68 mm^3, an increase of approximately 425% compared to N = 3000 r/min and a volume fraction of 25.33%. From the trend of the curves, there is a near-linear positive correlation between gas volume and rotational speed within the investigated range of 3000–4500 r/min. This suggests that in this specific speed interval, increasing the speed can continuously and effectively enhance cavitation yield without reaching a significant performance bottleneck.

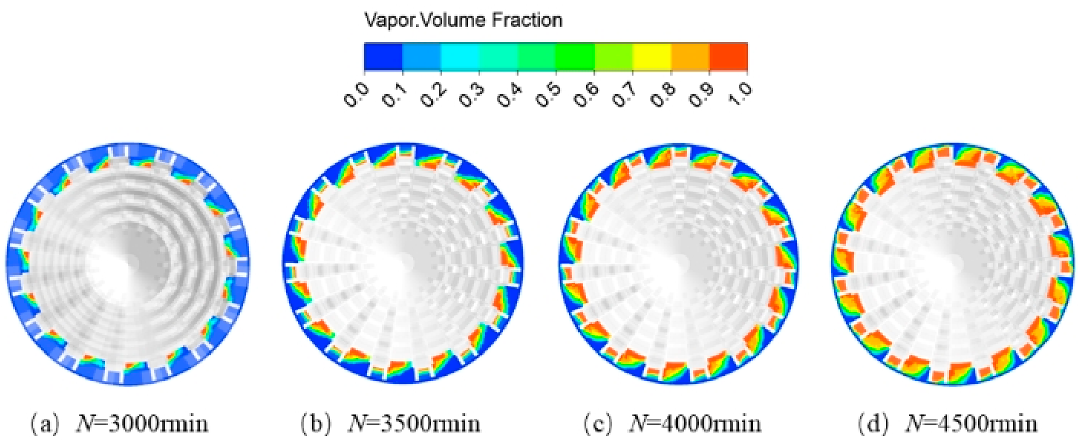

Figure 12: Gas phase contours inside the mover cavitation generator at different rotational speeds.

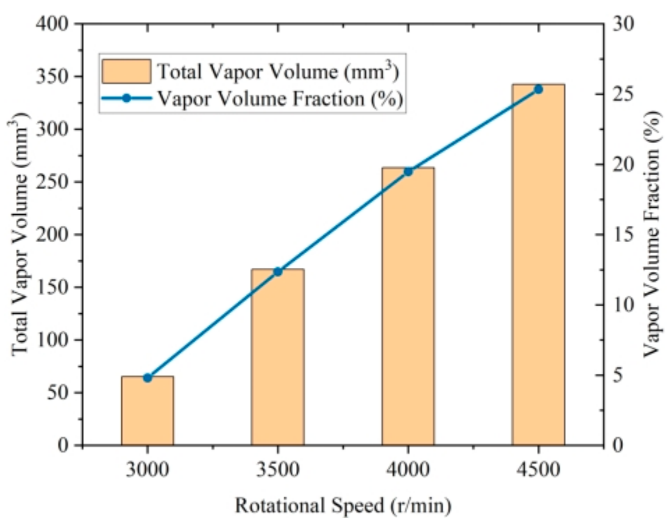

Figure 13: Diagram of rotor gas phase volume and gas phase volume fraction.

Fig. 14 shows the velocity distribution and motion trajectories of fluid pathlines inside the cavitation generator at different rotational speeds. The comparison indicates that variations in rotational speed have a significant influence on the flow-field characteristics. At a low rotational speed of N = 3000 r/min, the pathlines are relatively smooth and orderly, indicating that the overall flow velocity is low. The fluid particles mainly move regularly along the geometry of the flow passage, and interlayer mixing is weak. As the rotational speed increases to N = 4500 r/min, the velocity gradient between the rotor and stator teeth becomes increasingly large. Meanwhile, the pathline morphology changes from smooth to disordered, with obvious curling and vortex structures appearing inside the rotor grooves.

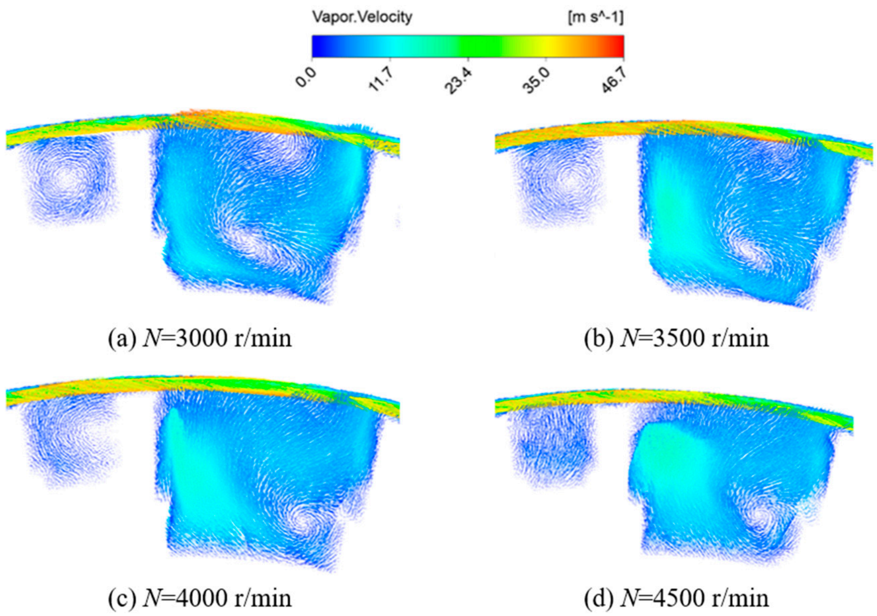

Figure 14: Trace plots of cavitation occurrence units on the mover at different rotational speeds.

3.3 Inactivation Experiments of E. coli Using the New Grooved-Tooth Cavitation Generator

The colony morphologies of *E. coli* at different cavitation treatment durations are shown in Fig. 15. Under identical inoculation and cultivation conditions, the number of *E. coli* colonies on the agar plates exhibits significant differences as the treatment time increases. Overall, the results demonstrate that the visible colony count on the plates gradually decreases with extended treatment time, indicating that the new grooved-tooth rotary cavitation generator possesses a distinct inactivation efficiency against *E. coli*. Furthermore, this inactivation effect shows a cumulative trend that strengthens over time.

Fig. 15a illustrates the control group at 0 min without cavitation treatment; the colonies are densely distributed with a large baseline count, serving as the initial reference level. Fig. 15b shows the *E. coli* solution after 10 min of treatment. Compared to the control group, the colony count significantly decreases, with only a small number of scattered colonies remaining on the plate. Fig. 15c presents the solution after 20 min of treatment, where the colony density is further reduced and the distribution becomes more sparse. Fig. 15d shows the solution after 30 min of treatment, at which point only a very few sporadic colonies are visible on the plate.

Consequently, under the conditions of this experiment, the three major effects of cavitation acting on the fluid have resulted in a significant disinfection of *E. coli* via the new grooved-tooth rotary cavitation generator. Moreover, a comparison of the culture media across the different time intervals confirms that increasing the cavitation treatment duration effectively enhances the cavitation performance within the experimental water samples.

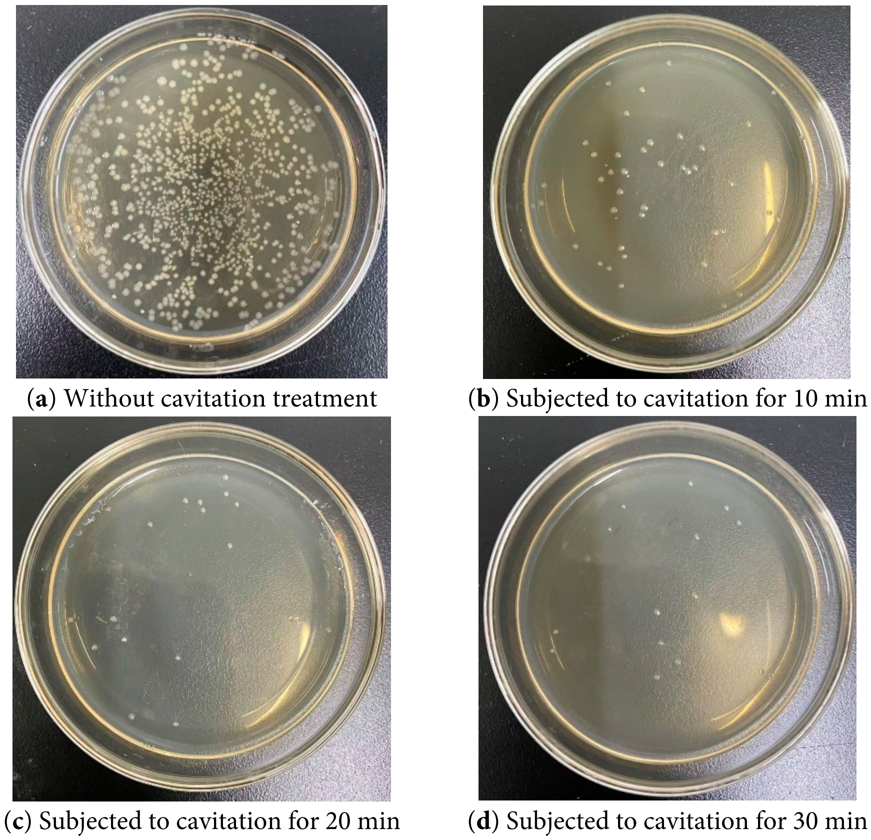

Figure 15: Colony images of Escherichia coli after treatment by the novel grooved-tooth rotating cavitation generator.

3.4 Degradation Experiments of Rhodamine B Using the New Grooved-Tooth Rotary Cavitation Generator

As illustrated in Fig. 16a–d, at any constant rotational speed, the degradation rate of Rhodamine B improves significantly as the radial clearance between the rotor and stator decreases. Specifically, as shown in Fig. 16d, at a rotational speed N of 4500 r/min, the degradation rate increases from 32.5% to 43.6% when the radial clearance L is reduced from 2.5 mm to 1 mm. The reduction in the radial gap between the rotor and stator enhances the rotor-stator interaction (RSI) effect. From a micro-scale flow field perspective, the narrower flow channels force the fluid to generate higher shear rates and pressure gradients the moment it passes between the teeth, thereby leading to a higher intensity of cavitation inception. Smaller clearances result in more intense turbulent disturbances within the flow field, significantly increasing the frequency of cavitation bubble collisions and collapses in the central region of the gap. This releases more energy through micro-jets and localized high temperatures and pressures, which accelerates the cleavage of the Rhodamine B molecular chains. From Fig. 16a–d, it can also be observed that at the same radial clearance, the degradation rate of Rhodamine B increases with the rise in rotor speed. The experimental results indicate that the rotor speed also has a positive impact on the degradation performance. As the speed increases, the frequency of cavitation events per unit of time increases accordingly. On one hand, higher speeds increase the pulsation excitation frequency of the rotor tooth grooves on the fluid, causing the flow field pressure to drop below the vapor pressure more frequently within extremely short intervals, which greatly enhances cavitation yield. On the other hand, the higher rotational speed inputs more mechanical energy, intensifying the impact strength at the moment of cavitation bubble collapse. The experimental results demonstrate that under the coupled conditions of L = 1 mm and N = 4500 r/min, the device reaches its optimal performance point where both physical shearing and chemical oxidation act in synergy.

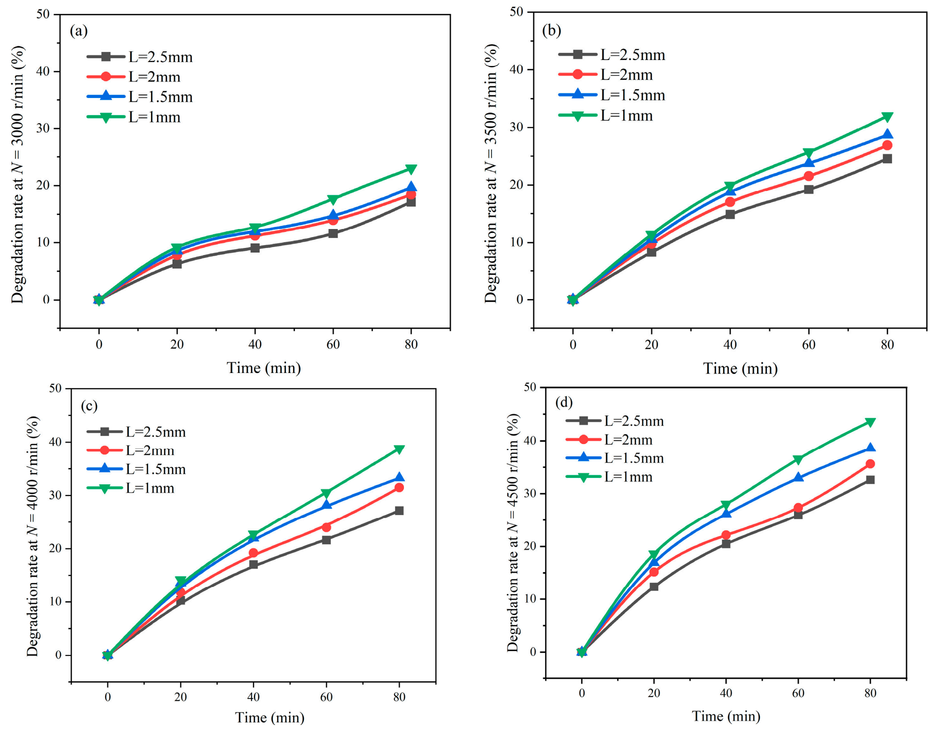

Figure 16: Degradation rate of Rhodamine B solution (**a**) rotational speed N of 3000 r/min; (**b**) rotational speed N of 3500 r/min; (**c**) rotational speed N of 4000 r/min; (**d**) rotational speed N of 4500 r/min.

As observed from the experimental phenomena shown in Fig. 17, at a constant rotor speed N of 4500 r/min, the fading effect of the pink color in the sample tubes becomes increasingly pronounced as the radial clearance L between the rotor and stator decreases. Specifically, the group with L = 1 mm exhibits the lightest chromaticity (color intensity), indicating that intense cavitation effects provide a superior degradation performance on organic dye molecules.

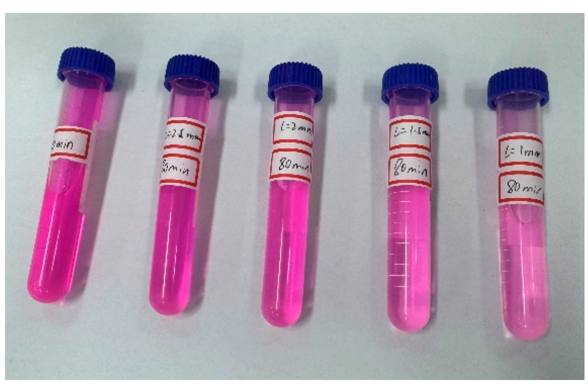

Figure 17: Comparison of solution concentration at different radial gaps between mover and stator for 80 min at N = 4500 r/min.

As observed from the experimental results shown in Fig. 18, at a fixed radial clearance L = 1 mm, the pink color of the solution gradually fades with the rise of rotational speed. The sample tube corresponding to N = 4500 r/min exhibits the most obvious decolorization effect, which proves that higher rotational speed can significantly boost the cavitation degradation performance of the device.

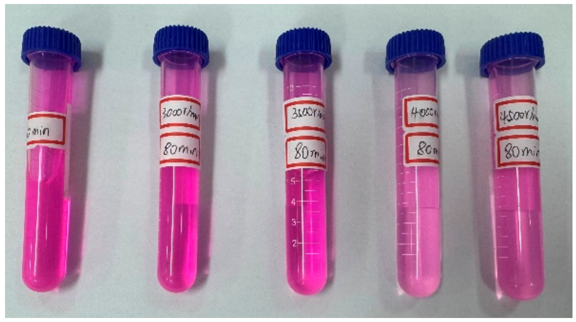

Figure 18: Comparison of solution concentration at different speeds for 80 min at L = 1 mm.

In summary, the cavitation effect and degradation performance of the rotary cavitation generator can be effectively enhanced by adjusting the radial clearance between the rotor and stator, as well as the rotor speed. The coordination of a small radial clearance and high rotational speed generates intense shear stress and violent pressure pulsations, which synergistically improve the degradation efficiency of pollutants. The operating characteristic data obtained in this study identifies the high-efficiency operational range of the device, providing a reliable theoretical basis and data support for subsequent industrial scale-up design. The results demonstrate that the combination of a smaller radial gap and a higher rotational speed effectively enhances flow field shearing and turbulent disturbance, thereby increasing the degradation rate of organic matter. This provides a scientific and quantitative basis for the engineering scale-up and performance regulation of the device.

3.5 Correlation Analysis between Simulation and Experimental Results of Cavitation Generator Performance Evolution

In this section, a correlation analysis was performed between the total gas phase volume obtained from numerical simulations and the Rhodamine B degradation rate obtained from experiments. The simulation results represent the cavitation evolution level within a transient period of 0.03 s, while the experimental results reflect the macroscopic cumulative treatment effect after 80 min of systemic circulation.

As shown in Fig. 19, at a constant speed of N = 4500 r/min both the simulated gas volume and the experimental degradation rate show a clear upward trend as the radial clearance L decreases from 2.5 mm to 1 mm, reaching their peak at L = 1 mm. This indicates that reducing the stator-rotor gap significantly intensifies the cavitation process. However, the growth rates were not perfectly synchronized: when L decreases from 2.5 mm to 2 mm, the gas volume increased significantly while the degradation rate rose more gradually. From 2.5 mm to 1.5 mm, the gas volume stabilized while the degradation rate continued to improve.

As shown in Fig. 20, at a fixed clearance of L = 1 mm, both parameters increased continuously as the rotational speed N rose from 3000 r/min to 4500 r/min. In the low-speed range (3000–3500 r/min), the gas volume increased rapidly whereas the degradation rate grew slowly. In the high-speed range (3000–3500 r/min), the two indicators exhibited consistent and synergistic growth characteristics.

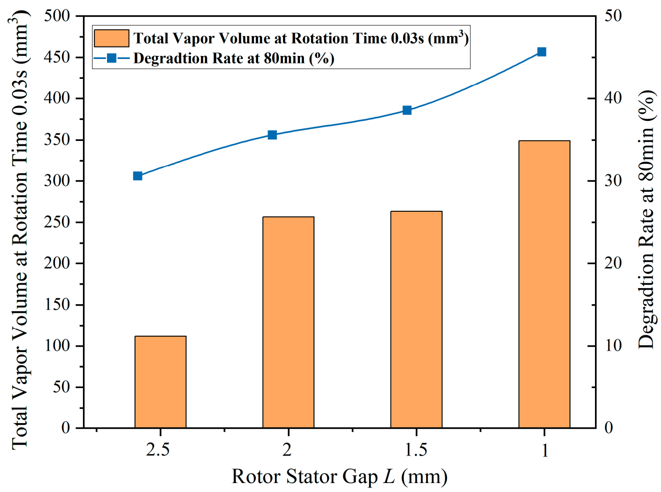

Figure 19: Variations of total gas phase volume and Rhodamine B degradation rate with radial distance of clearance between different rotors and stators.

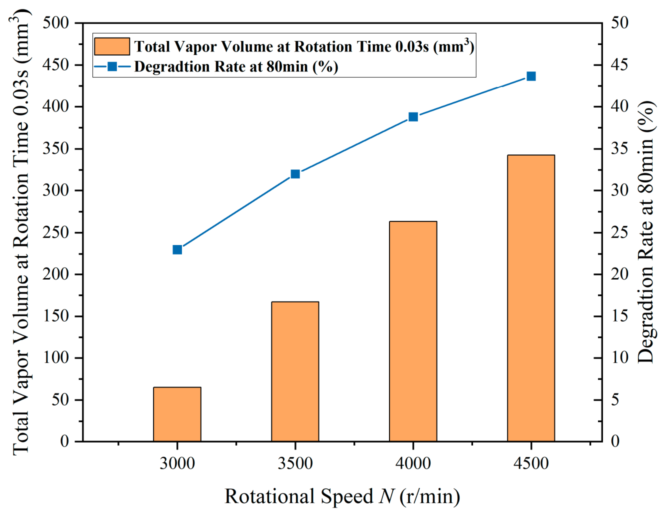

Figure 20: Variations of total gas volume and Rhodamine B degradation rate at different rotational speeds.

The reduction of radial clearance narrows the inter-tooth flow channel, significantly increasing the local shear rate and pressure gradient when fluid passes through the tooth gap. This expands the low-pressure zone below the saturated vapor pressure, activates more cavitation nuclei, and increases the total volume of cavitation bubbles. More violent bubble collapse will generate higher-intensity hydroxyl radicals (·OH) and stronger micro-jet shear force, which jointly improve the efficiency of organic molecular bond breaking and microbial cell damage. When the radial clearance decreases from 2.5 mm to 1 mm at 4500 r/min, the total vapor volume increases by 211.9%, and the corresponding 80-min Rhodamine B degradation rate increases from 32.5% to 43.6%. The fitting coefficient R^2 between simulated vapor volume and degradation rate reaches 0.94, verifying that the change of cavitation intensity caused by clearance adjustment is the core driving force for the improvement of pollutant removal efficiency. The increase of rotational speed increases the frequency of inter-tooth shear events per unit time; meanwhile, the enhanced centrifugal force strengthens the formation of low-pressure vortex cores inside the tooth grooves, further expanding the cavitation-prone area. The increase of rotational speed also raises the generation and collapse frequency of cavitation bubbles, enhancing the synergistic effect of physical shear and chemical oxidation in the system. When the rotational speed increases from 3000 r/min to 4500 r/min at L = 1.5 mm, the total vapor volume increases by 425%, and the corresponding 80-min Rhodamine B degradation rate increases from 18.2% to 35.7%. The high energy efficiency interval is maintained at 4000–4500 r/min, which is the recommended optimal operating range for engineering applications. The comparison reveals that the experimental degradation efficiency depends not only on the degree of cavitation evolution (gas volume) but also on bubble collapse intensity, the production efficiency of reactive radicals, flow field circulation characteristics, and cumulative time effects. Numerical simulations are more effective at revealing the direct influence of structural and operational parameters on cavitation behavior, while experimental results reflect comprehensive performance under multi-factor coupling.

The inactivation of *E. coli* is more dependent on the physical shear effect of micro-jets generated by cavitation bubble collapse, so it responds more significantly to the increase of rotational speed (which determines the frequency of shear events). The degradation of Rhodamine B relies more on the chemical oxidation of hydroxyl radicals, so it is more affected by the radial clearance (which determines the total volume of cavitation bubbles and the total yield of free radicals). In conclusion, although the simulated total gas phase volume and the experimental degradation rate are different evaluation metrics and lack a simple one-to-one linear relationship, their overall trends in response to structural L and operational N parameters are highly consistent, with identical optimal parameter points. This demonstrates that the numerical simulation method established in this study can effectively characterize the performance evolution of the rotary cavitation generator under various conditions, providing a reliable theoretical basis and data support for design optimization and operational control.

3.6 Comparison with Existing Studies and Critical Discussion

Existing studies on rotor-stator hydrodynamic cavitation reactors can be categorized into three mainstream technical routes, each with distinct technical characteristics and applicable scenarios. First, straight-tooth rotary reactors rely on inter-tooth throttling shear as the core cavitation mechanism. Featuring a simple structure and easy scale-up, most relevant studies focus on optimizing tooth ring arrangement and tooth geometry, but their cavitation form is relatively single and faces a bottleneck in energy efficiency improvement. Second, pinned-disk reactors generate cavitation through high-speed disturbance of numerous independent pin units. They deliver high cavitation intensity but suffer from high manufacturing and assembly costs as well as high risks of wear and clogging, making them more suitable for high-purity wastewater treatment. Third, groove-enhanced reactors improve cavitation performance via vortex-induced cavitation in recessed structures, with low processing cost and stable structure, which is recognized as a cost-effective optimization direction for tooth-type reactors. This study falls into the micro-structure enhanced cavitation technical route. By introducing micro-grooves on traditional tooth surfaces, it further explores the cavitation enhancement potential of tooth-type reactors.

For conventional tooth-type reactors, cavitation is exclusively generated by inter-tooth throttling shear. In contrast, the grooved-tooth structure proposed in this study retains the original inter-tooth shear cavitation, and additionally introduces in-groove vortex cavitation by inducing local micro-vortices through the tooth surface grooves, realizing the synergistic enhancement of shear cavitation and vortex-induced cavitation. This design idea of modifying the tooth surface micro-structure to introduce additional cavitation forms is a differentiated innovation different from existing optimization methods that mainly focus on tooth size adjustment and layout optimization, providing a new direction for the structural innovation of rotary cavitation generators.

Most existing studies adopt a single evaluation method, which has obvious limitations. Pure numerical simulation studies lack experimental validation, resulting in limited engineering reference value of performance conclusions. Experimental studies mostly use a single pollutant as the evaluation indicator, which is susceptible to interference from pollutant properties and may lead to deviation in results. This study constructs a three-dimensional evaluation system combining transient flow field simulation, refractory organic pollutant degradation and microbial inactivation, which cross-verifies the cavitation performance from three dimensions: flow mechanism, chemical oxidation effect and biological disinfection effect. This system not only improves the reliability of performance conclusions, but also provides a more comprehensive reference framework for performance benchmarking across different studies.

It should be objectively noted that this study still has certain limitations. The current work is only a mechanistic verification of a single new structure at the bench scale, and parallel comparative tests with other typical structures have not been carried out on a unified test platform with identical boundary conditions. The performance data obtained in this study are only used to characterize the relative influence law of structural and operating parameters, and cannot be directly used for absolute performance benchmarking with industrial-grade devices of different scales and structures.

4 Conclusion

This study developed a novel grooved-tooth rotary hydrodynamic cavitation generator and validated its performance via numerical simulations and experiments. Results revealed that reducing the rotor-stator radial clearance to 1 mm and raising the rotational speed to 4500 r/min produced the strongest cavitation effect, with the total gas phase volume reaching 349.03 mm^3 and the Rhodamine B degradation rate peaking at 43.6%. The device exhibited satisfactory disinfection capacity, achieving continuous inactivation of *E. coli* as treatment time increased. Simulated total gas phase volume shared consistent variation trends and optimal operating points with experimental data, verifying the reliability of the adopted numerical model. The proposed grooved-tooth structure effectively enhances cavitation intensity and energy utilization. Future work will focus on optimizing tooth profiles, exploring combined cavitation technologies, and conducting on-site pilot tests to further promote the practical application of this equipment in wastewater treatment.

Acknowledgement: The authors would like to express sincere gratitude to the supervisor for valuable guidance and constructive suggestions throughout the whole research and manuscript preparation. In addition, we thank all laboratory colleagues for their assistance in simulation data processing and manuscript polishing.

Funding Statement: The authors gratefully acknowledge the support provided by Jiangsu Province's "Blue Project" (Su Teacher's Letter [2024] No. 2), Sixth batch of external teacher doctoral studio scientific research projects of Nantong Institute of Technology (WP202505) and Nantong Institute of Technology Science and Technology Innovation Fund (KCTD004).

Author Contributions: All authors have contributed to the development of the research and the elaboration of this paper. Hong Qi: Investigation, Numerical simulation, Writing—original draft. Jun Zhang: Conceptualization, Methodology, Writing—original draft. Xinyao Hu: Experimental work, Data curation. Liming Qian: Experimental validation, Formal analysis. Peiyu He: Conceptualization, Writing—review & editing, Supervision, Funding acquisition. All authors reviewed and approved the final version of the manuscript.

Availability of Data and Materials: All datasets generated in this study are available from the corresponding author upon reasonable request.

Ethics Approval: Not applicable.

Conflicts of Interest: The authors declare no conflicts of interest.

Nomenclature

$C_{1\varepsilon}$	empirical constants
$C_{2\varepsilon}$	empirical constants
C_{cond}	evaporation coefficient
C_{RhB}	mass concentration of Rhodamine B solution
C_{vap}	condensation coefficient
$\vec{F}$	volumetric force
$\vec{g}$	gravitational acceleration vector
$\dot{m}^{+}$	source terms for mass exchange between the gas and liquid phases per unit time, referred to as the vaporization term
$\dot{m}^{-}$	source terms for mass exchange between the gas and liquid phases per unit time, referred to as the condensation term
M	dilution factor
n	torque
N	number of effective colonies on the plate
R_B	radius of a single cavitation bubble
u	molecular dynamic viscosity
u_t	turbulent dynamic viscosity
v_m	mass-averaged velocity
p	flow field pressure
P	static pressure
P_k	turbulence kinetic energy generated by velocity gradients
p_v	micro-liquid saturation vapor pressure
T	rotor speed
V	inoculation volume
V_{vapor}	total cavitation bubble volume in the computational domain
V_{total}	total volume of the computational domain
Y_{RhB}	absorbance value
α	cavitation rate
α_{nuc}	cavitation nuclei volume fraction
α_{v}	vapor phase volume fraction
η	cavitation energy efficiency
μ_m	mixture molecular viscosity
μ_l	liquid dynamic viscosity
μ_v	vapor dynamic viscosity
ε	turbulence dissipation rate
k	turbulence kinetic energy
ρ	density of the turbulent mixture
ρ_l	liquid phase density
ρ_m	mixed density of the water phase and the bubble phase
ρ_v	vapor phase density
σ_k	turbulent Prandtl number for the turbulence kinetic energy k

References

1. Kallawar G, Thakare N, Bonde S, Barai D, Bhanvase BA, Sonawane A, et al. Exploring sonochemical synthesis for photocatalyst nanocomposites in water and wastewater treatment: an in-depth review. J Clean Prod. 2024;485:144279. [CrossRef].
2. Huang X, Yang D, Song L, Jiang Y. Degradation of antibiotics in aquaculture seawater: a treatment based on ozone assisted with hydrodynamic cavitation. Water. 2025;17(4):566. [CrossRef].
3. Sun H, Li J, Zhuang L, Zhang Y, Zhou Z, Sun J, et al. Ultrasonic cavitation transforms organic matter to achieve reduction of excess sludge and recycling of carbon sources. Toxics. 2025;13(11):941. [CrossRef].
4. Luo W, Tang L, Yan Y, Shi Y. Optimal structural parameters for a plastic centrifugal pump inducer. Fluid Dyn Mater Process. 2023;19(4):869–99. [CrossRef].
5. Li D, Xi Y, Li R, Hong F, Yuan X, Huang D, et al. Investigation on the mechanism of Cr(VI) reduction driven by hydrodynamic cavitation: comprehensive analysis of the bubble dynamics and free radical generation. Sep Purif Technol. 2025;368:133058. [CrossRef].
6. Su W, Meng W, Zhao Y, Wu J, Sun Y. Research on an acoustic judgment method for the incipient cavitation of model hydraulic machinery runner blades. Matéria. 2023;28(3):e20230154. [CrossRef].
7. Zhu X, Wang J. Hydrodynamic cavitation enhanced SR-*Aops* degradation of organic pollutants in water: a review. Fluid Dyn Mater Proc. 2024;20(4):671–92. [CrossRef].
8. Golshaei R, Heyat Davoudian S, Toyran E, Kestek E, Kaur A, Priyadarshi A, et al. Novel concept of hydroxyl radical generation in hydrodynamic cavitation on a chip. Chem Eng J. 2025;517:164356. [CrossRef].
9. Arya SS, More PR, Ladole MR, Pegu K, Pandit AB. Non-thermal, energy efficient hydrodynamic cavitation for food processing, process intensification and extraction of natural bioactives: a review. Ultrason Sonochem. 2023;98:106504. [CrossRef].
10. Zhang H, Hu S, Li S, Zhang L. Synergistic mechanism of ultrasonic cavitation and advanced oxidation: free radical path optimization and advanced treatment of industrial wastewater. J Environ Chem Eng. 2025;13(4):117232. [CrossRef].
11. Gągol M, Przyjazny A, Boczkaj G. Wastewater treatment by means of advanced oxidation processes based on cavitation—a review. Chem Eng J. 2018;338:599–627. [CrossRef].
12. Han H, Chen M, Sun C, Han Y, Xu L, Zhao Y. Synergistic enhancement in hydrodynamic cavitation combined with peroxymonosulfate Fenton-like process for bpa degradation: new insights into the role of cavitation bubbles in regulation reaction pathway. Water Res. 2025;268(Pt A):122666. [CrossRef].
13. Pawar SK, Mahulkar AV, Pandit AB, Roy K, Moholkar VS. Sonochemical effect induced by hydrodynamic cavitation: comparison of venturi/orifice flow geometries. AlChE J. 2017;63(10):4705–16. [CrossRef].
14. Sun X, Xuan X, Song Y, Jia X, Ji L, Zhao S, et al. Experimental and numerical studies on the cavitation in an advanced rotational hydrodynamic cavitation reactor for water treatment. Ultrason Sonochem. 2021;70:105311. [CrossRef].
15. Guo C, Li J, Li S, Li H, Huang Z. Self-excited pulsation performance and dual-cavitation synergistic mechanism of the angular Helmholtz cavitation jet nozzle. Phys Fluids. 2025;37(5):053315. [CrossRef].
16. Xia G, Manickam S, Yoon JY, Boczkaj G, Wang W, Wang B, et al. Technological advances and applications of rotational hydrodynamic cavitation reactors for process intensification: a comprehensive review. Chem Eng J. 2025;522:167152. [CrossRef].
17. Sun X, Yang Z, Wei X, Tao Y, Boczkaj G, Yoon JY, et al. Multi-objective optimization of the cavitation generation unit structure of an advanced rotational hydrodynamic cavitation reactor. Ultrason Sonochem. 2021;80:105771. [CrossRef].
18. Zhang X, Lin R, Zhang L, Chen J, Li M, Wang Y. Numerical investigation of effect of geometric parameters on performance of rotational hydrodynamic cavitation reactor. Ultrason Sonochem. 2024;103:106790. [CrossRef].
19. Gostiša J, Širok B, Repinc SK, Levstek M, Stražar M, Bizjan B, et al. Performance evaluation of a novel pilot-scale pinned disc rotating generator of hydrodynamic cavitation. Ultrason Sonochem. 2021;72:105431. [CrossRef].
20. Badve M, Gogate P, Pandit A, Csoka L. Hydrodynamic cavitation as a novel approach for wastewater treatment in wood finishing industry. Sep Purif Technol. 2013;106:15–21. [CrossRef].

21. Shen X, Han W, Li R, Yang S, Nan H, Bai L, et al. Investigation of the impact load characteristics of micro-jet induced by cavitation collapse on rigid wall surface. Chem Eng J. 2024;501:157686. [CrossRef].
22. Zhu J, Wu G, Duan X, Li X, Tang X. Numerical studies on applications of cavitation models in water hammer-induced cavitating flows in pipelines. Phys Fluids. 2023;35(9):095129. [CrossRef].
23. Jia X, Zhou H, Zhu Z, Lin Z. Study on pressure fluctuation characteristics induced by cavitation flow in an axial flow pump. Phys Fluids. 2025;37(8):084124. [CrossRef].
24. Wei C, Zhang H, Shi W, Yang Y, Tan L, Wu X, et al. Cavitation control in mixed-flow pumps through blade perforation. Fluid Dyn Mater Proc. 2026;22(2):1–10. [CrossRef].